International Journal of Nanoelectronics and Materials
IJNeaM
ISSN 1985-5761 | E-ISSN 2232-1535

Kinetic release mechanism of the composite poly(D,L-Lactide)/natural clay nanoparticles loaded with *Moringa Oleifera* leaves extract

Rahimah Othman [a,b] *, Tanushaa Gail Gabriel [a], Au Jian Ding [a], Mohd Irfan Hatim Mohd Dzahir [a], Nor Farahiyah Aman Nor [c], and Kehinde Adenike Oyewole [d]

[a]*Faculty of Chemical Engineering & Technology, Universiti Malaysia Perlis, Kompleks Pusat Pengajian Jejawi, 02600 Arau, Perlis, Malaysia*
[b]*Centre of Excellence for Biomass Utilization, Universiti Malaysia Perlis (UniMAP), Perlis, Malaysia*
[c]*Institute of Bioproduct Development, Universiti Teknologi Malaysia, 81310 Johor Bahru, Malaysia*
[d]*Department of Chemical Engineering, Osun State University, Osogbo, Nigeria*
** Corresponding author. Tel.: +6012-2683052; e-mail: rahimah@unimap.edu.my*

Received 12 September 2025, Revised 01 October 2025, Accepted 10 October 2025

ABSTRACT

Nanoparticulization provides distinctive advantages such as controlling the drug release rate and designing to reduce the side effects of the drug to the human body. However, the sustained release of *Moringa Oleifera* (MO) bioactives remains challenging, as the kinetic mechanism from natural clay/PLA nanoparticles is not yet fully elucidated. This study investigates the kinetic release and mechanism of composite poly(D,L-lactide) (PLA)/natural montmorillonite (MMT) nanoparticles (NPs) loaded with MO leaf extract through *in vitro* testing. To investigate the drug release profile, MO leaves need to be extracted by Soxhlet extraction and freeze-dried. The total phenolic content (TPC), total flavonoid content (TFC), 1,1-diphenyl-2-picrylhydrazyl (DPPH) assay, and 2,2'-azino-bis-[3-ethylbenzothiazoline sulphonate] (ABTS) radical cation decolorization assay for MO extract are 372.81 mg GAE/g, 90.89 mg QE/g, 91.68% and 85.1%, respectively. For MO powder, the TPC, TFC, DPPH, and ABTS are 373.37 mg GAE/g, 92.15 mg QE/g, 94.02%, and 89.42%, respectively. Freeze-dried MO powder was encapsulated in PLA/MMT to sustain its release at varying pH levels (2, 5.5, and 7.4). Fixed parameters included an aqueous-to-organic phase ratio of 10, a stirring speed of 1200 rpm, 1 wt/wt% MMT, and 5 wt/wt% MO. MO loading and encapsulation efficiencies were 12% and 16% for PLA-loaded MO NPs and 74% and 84% for composite PLA/MMT-loaded MO NPs, respectively. The kinetic release mechanisms of these PLA/MMT-loaded MO NPs were then validated using the zero-order, first-order, Higuchi, and Korsmeyer-Peppas models, respectively. Characterization via XRD, FTIR, and SEM revealed monodispersed spherical NPs with average sizes of 200 nm, 270 nm, and 240 nm for PLA blank NPs, PLA-loaded MO NPs, and PLA/MMT-loaded MO NPs, respectively. The release mechanism followed Fickian diffusion, and the drug release profile aligned with the Korsmeyer-Peppas model. This work provides a potential basis for the synthesis, characterization, and kinetic release processes needed to create sophisticated and sustained pharmacological formulations.

Keywords: *Kinetic release mechanisms, Nanoprecipitation, Nanoparticles, Moringa Oleifera leaves, Poly(D,L-lactide), Montmorillonite*

1. INTRODUCTION

The advancement of nanotechnology has significantly influenced the field of drug delivery, offering innovative solutions for controlled and targeted therapeutic applications. Biodegradable polymers, particularly poly(D,L-lactide) (PLA), have garnered attention due to their favorable biocompatibility and degradation profiles, making them suitable candidates for drug encapsulation and delivery systems. Incorporating natural clay minerals like montmorillonite (MMT) into PLA matrices has been shown to enhance mechanical strength and modulate drug release profiles, thereby improving the efficacy of the delivery system [1]. Furthermore, the integration of phytochemicals, such as those derived from *Moringa Oleifera* (MO) leaves, offers a sustainable approach to developing multifunctional nanocarriers with inherent therapeutic properties.

Despite advancements in nanotechnology, challenges persist in achieving optimal drug loading efficiency, controlled release kinetics, and physiological stability of nanocomposites. Encapsulation of hydrophilic phytochemicals, such as those from MO leaves, into hydrophobic matrices like poly(D,L-lactide) (PLA) has frequently resulted in low loading efficiencies and uncontrolled release behavior [2]. Previous studies have also reported biphasic release patterns characterized by an initial burst followed by a sustained release phase, which is suboptimal for certain therapeutic applications that require steady-state plasma concentrations [2, 3]. Furthermore, many of these nanocarriers lack structural and chemical stability under physiological conditions, which compromises therapeutic efficacy. Therefore, there is a pressing need to explore novel formulations capable of improving encapsulation efficiency, enhancing release control, and maintaining bioactive stability. One promising strategy involves the integration of MO extracts into PLA/natural MMT nanocomposites, which has been shown to improve mechanical and barrier properties while also allowing sustained release of therapeutic agents [4]. The rich antioxidant and antimicrobial properties of MO further

enhance the health-promoting potential of these systems, supporting their application in biomedical and nutraceutical fields [5]. Thus, understanding the kinetic release mechanisms and optimizing nanoparticle formulation parameters are critical steps toward the development of reliable and effective nanocarrier systems.

Herbal bioactives encapsulated in nanoparticles have gained substantial attention due to their ability to enhance stability, bioavailability, and controlled delivery of phytochemicals [6, 7]. Previous studies, like the study of curcumin-loaded casein nanoparticles, were reported to show sustained release with up to 80% cumulative release over 72 hours, and the release kinetics followed the Korsmeyer–Peppas model with an "*n*" value of 0.45, indicating Fickian diffusion [8]. In a similar study, thymol encapsulated within mesoporous silica nanoparticles demonstrated a cumulative release of 70% over 48 hours at pH 7.4, and the release data fit well to the Higuchi model (R^2 = 0.983), confirming diffusion-controlled kinetics [9]. Silver nanoparticles synthesized using *Inula viscosa* extract were also characterized, with particle formation conforming to a first-order kinetic model and a calculated rate constant of 0.032 min^{-1}, highlighting a predictable synthesis and release profile [10]. In another report, polyphenol-rich plant extracts encapsulated in pectin nanoparticles exhibited biphasic release behavior, with an initial burst (30% in 4 hours) followed by a sustained release phase up to 96 hours; the Korsmeyer–Peppas model (n = 0.52) and Higuchi model best described the release kinetics [11]. Furthermore, green tea polyphenols encapsulated in chitosan nanoparticles showed 90% release over 72 hours, with strong alignment to the Peppas–Sahlin model, indicating the combined effect of diffusion and polymer relaxation [12]. These findings suggest that encapsulation techniques, nanoparticle composition, and pH conditions significantly influence release mechanisms, and that modelling these mechanisms is crucial to predict in vivo performance.

Thus, in this study, PLA and natural MMT composite nanoparticles loaded with MO leaf extract are synthesized and characterized to address the need for effective, natural-based drug delivery systems. The encapsulation efficiency and loading capacity are evaluated to determine the suitability of the PLA/MMT matrix for sustaining and protecting sensitive phytochemicals during release. The release behavior of the bioactive compounds is examined under different pH conditions (2.0, 5.5, and 7.4) to mimic gastrointestinal and physiological environments and to establish pH-responsive characteristics. The kinetic release mechanisms are analyzed using established mathematical models, including the Korsmeyer–Peppas and Higuchi models, to assess the diffusion and transport phenomena governing release. The antioxidant and antimicrobial activities of the released compounds are further assessed to verify the therapeutic efficacy over time. This project significantly lies in improving bioavailability, minimizing burst release, and improving the stability of herbal-derived bioactive compounds, which are key challenges in phytochemical delivery systems.

2. MATERIALS AND METHODS

2.1. Materials

Poly(D,L-lactide) (PLA) and acetone (with a purity of ≥ 99.98%) were obtained from Sigma-Aldrich. Additional chemicals such as methanol, MMT, quercetin, gallic acid, Folin-Ciocalteu reagent, aluminum chloride, sodium nitrate, sodium carbonate, and polyvinyl alcohol (PVA) were obtained from R&M Chemicals, Malaysia, with a purity above 90%. PVA was used as the stabilizer, which prevents agglomeration of NPs. Distilled water was employed as the aqueous component in both the Soxhlet extraction and nanoprecipitation processes. MO leaves were collected from constant shrub regions in Perlis, ensuring uniformity in size (approximately 10–15 mm × 10 mm) and color. The organic phase consisted of a homogeneous solution containing 1 mg/mL of the polymer, along with specific proportions of MO and MMT dissolved in acetone. For nanoprecipitation, the aqueous phase was prepared by blending 2 wt% of polyvinyl alcohol into distilled water. Methanol, acetone, ethanol, and ethyl acetate were applied for the extraction process, respectively. While, for antioxidant compounds and their assay analyses, sodium chloride, quercetin, aluminium chloride, gallic acid, Folin-Ciocalteu reagent, sodium carbonate, 2,2-diphenyl-1-picrylhydrazyl (DPPH), and 2,2'-azino-bis-[3-ethylbenzothiazoline sulphonate] (ABTS) were used. For the NPs release study, phosphate buffered saline (PBS), hydrochloric acid, sodium hydroxide, and monobasic potassium phosphate were utilized.

2.2. Methods

2.2.1. MO Extract Powder Preparation

Fresh MO leaves, including their stems, were harvested and separated, then thoroughly washed with tap water to remove any dirt or impurities. They were next soaked in a 1% sodium chloride solution for 10 minutes, followed by another round of washing with tap water to ensure complete removal of impurities and sodium chloride. The leaves were air-dried at room temperature for 3 days until fully dried. Once dried, they were finely powdered through blending and sieving, achieving particle sizes ranging from 200 to 250 µm, and stored in an airtight container. The extraction of 5 g of MO powder was produced, as per the method outlined by Marimuthu *et al.* [13], involving Soxhlet extraction with a solvent mixture of acetone, methanol, and distilled water. This extraction process was conducted at 100°C for 200 minutes. After extraction, the resulting extracts were concentrated using a rotary evaporator for 20 minutes and then stored in a refrigerator at 5 to 10°C. The concentrated MO extract underwent freeze-drying using a Lanconco FreeZone 4.5 Liter −50C Benchtop Freeze Dryer at −49°C for 72 hours. The resulting freeze-dried MO powder was obtained and promptly stored in a desiccator for future use.

2.2.2. Total Phenolic Content (TPC) Analysis

The determination of Total Phenolic Content (TPC) was conducted employing the Folin-Ciocalteau colorimetric method, utilizing gallic acid as the standard internal reference. A calibration curve for gallic acid was constructed, yielding a linear equation of $y = 0.002x + 0.0003$, with an R^2 value of 0.99. Sample preparation involved combining 0.15 mL of extract and 0.3 mL of Folin-Ciocalteau reagent in 12 mL of distilled water. The mixture was then allowed to be incubated at room temperature for 5 minutes. Following incubation, 2 mL of 20% sodium carbonate was added, and the resulting solution was incubated once more in darkness for 25 minutes. Subsequent to incubation, the absorbance was measured at a wavelength of 765 nm using a UV-visible spectrophotometer (Thermo Spectronic GENESYS 20, USA). The phenolic content of the sample, expressed in milligrams of gallic acid equivalent (GAE) per gram of extract, was determined utilizing the calibration curve based on Equation (1).

$$\text{TPC}\left(\text{GAE}\frac{\text{mg}}{\text{g}}\right) = C \times V/g \quad (1)$$

where C is the concentration of gallic acid equivalent from the standard curve (μg/mL), V is the volume of the standard/extract sample used (mL), and g is the weight of the extract (g).

2.2.3. Total Flavonoid Content (TFC) Analysis

The determination of Total Flavonoid Content (TFC) was carried out using the aluminum chloride colorimetric method, with quercetin employed as the standard internal reference. A calibration curve was generated, yielding a linear equation of $y = 0.007x - 0.002$ ($R^2 = 0.99$). For sample preparation, 0.75 mL extract and 0.25 mL of 50% sodium nitrate were combined with 3 mL of distilled water. The mixture was then incubated at room temperature for 5 minutes. Following this, 0.15 mL of 10% aluminum chloride was added, and the solution was left to stand in darkness for 20 minutes. Subsequently, the absorbance reading was measured at 415 nm using a UV-visible spectrophotometer (Thermo Spectronic GENESYS 20, USA). The TFC of the sample, expressed in milligrams of quercetin equivalent (QE) per gram of extract, was determined utilizing the calibration curve based on Equation (2).

$$\text{TFC}\left(\text{QE}\frac{\text{mg}}{\text{g}}\right) = C \times V/g \quad (2)$$

where C is the concentration of quercetin equivalent from the standard curve (μg/mL), V is the volume of the standard/extract sample used (mL), and g is the weight of the extract (g).

2.2.4. 2,2-diphenyl-1-picryhydazyl (DPPH) Free Radical Scavenging Activity Analysis

0.0098 g of DPPH (MW of 394.32 g/mol) was dissolved in 25 mL of ethanol, resulting in a concentration of 1 mM. A working solution was then made with a final concentration of 60 μM by diluting the stock solution, combining 1.5 mL of it with 25 mL of ethanol. For the sample, 2.5 mL of the DPPH working solution was mixed with 200 μL of the MO extract, while for the control, 2.5 mL of the DPPH working solution was mixed with 200 μL of distilled water. The sample and control were kept in the dark for 30 minutes to allow the reaction to occur. A UV–visible spectrophotometer (Thermo Spectronic GENESYS 20, USA) was set at 517 nm wavelength for this analysis, with ethanol utilized as the blank sample to minimize signal interference. DPPH free radical scavenging activity of the MO extract was calculated as follows based on Equation (3) [14].

$$\text{DPPH}\ (\%) = \left[\frac{A_{0(\text{control})} - A_{1(\text{sample})}}{A_{0(\text{control})}}\right] \times 100 \quad (3)$$

where A_0 is the absorbance reading for the control, while A_1 is the absorbance reading for the sample.

2.2.5. 2,2′-azino-bis(3-ethylbenzothiazoline-6-sulfonic acid) (ABTS) Assay Analysis

0.096 g of ABTS was dissolved in 25 mL of water to create a 7 mM solution. 0.016 g of potassium persulfate was next added to 25 mL of water, resulting in a 2.45 mM solution. These solutions were mixed and allowed to stand for 12–16 hours at room temperature in the dark to form the ABTS radical cation (ABTS+). For the blank sample, distilled water was used to correct for any background absorbance. For ABTS control, the ABTS+ solution was diluted with methanol until it reached an absorbance of 0.706 at 734 nm, determined through trial and error. Subsequently, 1 mL of the MO extract was added to 1 mL of the diluted ABTS+ solution, and the absorbance was measured after 7 minutes of initial mixing. Both the extract sample and blank sample were transferred into a spectrophotometer, and their absorbance was recorded at a wavelength of 734 nm [15]. Three runs have been conducted for each sample. The inhibition of absorbance of the sample was calculated using Equation (4).

$$\%\ \text{Inhibition} = \left[\frac{A_{0(\text{control})} - A_{s(\text{sample})}}{A_{0(\text{control})}}\right] \times 100 \quad (4)$$

where, A_0 is the absorbance of control ($ABTS^{+}\bullet$ only), and A_S is absorbance with antioxidant.

2.2.6. Synthesis of PLA/MMT-loaded MO NPs

The creation of nanoparticles containing MO leaves within a poly(D,L-lactide) (PLA)/MMT matrix was carried out using the nanoprecipitation method, as illustrated in Figure 1. Minor adjustments were made to the procedure described by Reis *et al.* [16]. In this approach, the organic phase was injected into the aqueous phase with a NE-300 Just Infusion syringe pump under uniform stirring conditions. The aqueous phase turned cloudy upon contact with the organic phase, indicating nanoparticle formation, likely due to the swift exchange of solvents [17]. After nanoparticle formation, acetone was left to evaporate overnight at room temperature.

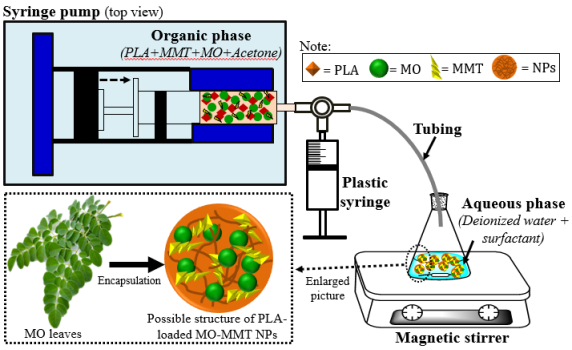

Figure 1. Schematic diagram of the PLA/MMT-loaded MO NPs nanoparticle formation

2.2.7. Encapsulation Efficiency Determination

To determine the encapsulation efficiency of the synthesized PLA/MMT-loaded MO NPS NPs, the NPs undergo centrifugation at 4500 rpm for 3 hours. Subsequently, the supernatant obtained post-centrifugation is extracted and analyzed for concentration using a UV-visible spectrophotometer (Thermo Spectronic GENESYS 20, USA) at 765 nm wavelength. The concentration of Total Phenolic Content (TPC) in the supernatant is then determined utilizing the calibration curve obtained in Section 2.2.2. The encapsulation efficiency (% EE_{TPC}) is subsequently calculated using Equation (5).

$$EE_{TPC}\ (\%) = 1 - \left[\frac{\text{TPC on NPs surface}}{\text{TPC of NPs}}\right] \times 100 \qquad (5)$$

2.2.8. Kinetics and Release Mechanisms Studies

The *in vitro* release of MO from the natural-clay/ poly(ε-caprolactone) (PLA/MMT) composite was conducted using 3 release mediums with different pHs, (i) pH 7.4 refers to blood environment, (ii) pH 2.0 stimulates the gastric solution, (iii) pH 5.5 stimulates the intestine digestion. The PLA/MMT-loaded MONPs were inserted into the release medium (in a test tube) and incubated at 37°C and 75 rpm of agitation speed, which mimicking the human body conditions. After certain interval times (20–180 minutes), of incubation, the supernatant was taken out from the test tube and measured by the UV-vis spectrophotometer [2].

Table 1 summarizes the kinetic release models with respective equations and parameters definition.

2.2.9. Physicochemical Analyses of MO-loaded MMT/ PLA NPs

(i) Fourier Transform Infrared Spectroscopy (FTIR) Analysis. The functional group of the synthesized PLA/MMT loaded-MO NPs, FTIR (Perkin Elmer FTIR Spectrum RXI Spectrometer) analysis was carried out. Three types of samples were analyzed; blank PLA NPs, PLA loaded-MO NPs and PLA/MMT loaded-MO NPs. All the samples were combined with bromide (KBr) as the sample preparation method before subjecting to FTIR analysis. The wavelength used for the spectrum absorption is in the range of 400–4000 cm^{-1}.

(ii) X-ray diffraction analysis (XRD) Analysis. A Bruker D2 Phaser (Germany) diffractometer was used to perform wide angle X-ray diffraction. Samples were exposed to CuK radiation (40 kV, 20 mA) throughout a 2θ range of 10° to 40°, with a step size of 0.02°, an acquisition time per step of 5 s, and a scanning speed of 0.5° min^{-1}. The samples were evenly placed onto a circular mould with a 20 mm diameter and a 1 mm thickness at room temperature. Six different samples were analysed, including pure MO, pure MMT, pure PLA, physical mixture, PLA/MMT-loaded MO NPs and PLA-loaded MO NPs. The XRD diffractograms were obtained from the analysis and compared.

(iii) Scanning Electron Microscopy (SEM) Analysis. SEM was used to analyse the surface morphology of the PLA/MMT loaded-MO NPs. To increase the generation of secondary electrons and provide a conductive surface, platinum (Pt) was applied to the surfaces of the prepared materials using an Auto Fine Coater JFC 1600, Japan, prior

Table 1. The kinetic mechanism models with respective equations and parameters

Model	Equation	Parameters Definition
Zero Order Release Kinetic Model	$D_t = D_0 + k_0 t$	D_t: Amount of drug dissolved D_0: Initial drug amount in the solution k_0: Zero order release rate constant t: Time
First Order Release Kinetic Model	$\log C_0 - \log C_t = k_1 t/2.303$	C_0: Initial drug concentration C_t: Concentration at time t k_1: First order rate constant t: Time
Higuchi Model	$Q = k_H t^{1/2}$	Q: Amount of drug released at time t k_H: Higuchi constant t: Time
Korsmeyer-Peppas Model	$M_t/M_\alpha = k_P t^n$	M_t / M_α: Fraction of drug released at time t k_P: Korsmeyer-Peppas constant t: Time n: Release index

to observation to create a conductive layer of metal which is required for non-conductive samples to improve the imaging of the samples produced. The chamber of the JEOL's JSM-6010 LV SEM, Japan with secondary electrons (SE) detector at 15 kV was used for sample imaging.

3. RESULTS AND DISCUSSION

3.1. MO Leaves Extract: Moisture Content

The pre-treated MO leaves were air-dried at room temperature for 4 days to reduce the moisture content within the leaves. The initial moisture content (MC) of powdered MO was detected at 91.28% (wet basis), the 8.72% of dry matters, which significantly might affect its MC quality after blending process. Thus, this drying process is needed to prolong the shelf-life of MO leaves and avoid leakage of flavonoids from the leaves and protect cell wall integrity [18].

3.2. MO Leaves Extract: TPC and TFC

The type of extraction in this study was Soxhlet extraction, which was optimized by Marimuthu *et al.* [13] with methanol, acetone, and distilled water. The TPC value obtained in this study is 372.81 mg GAE/g, and the TFC value is 90.885 mg QE/g. TPC is a bit higher than Devi's results, which reported that the TPC value was 313.265 mg GAE/g, while the TFC value is almost similar to her result, which stated 90.268 mg QE/g as the TFC value. The TPC and TFC values are significantly higher than other studies, as concluded in Table 2. The different values are due to the extraction time that most likely affected the TPC value, while the concentration of solvent will influence the TFC values [19]. The TPC and TFC values of MO powder are 373.37 mg GAE/g and 92.146 mg QE/g, respectively. To compare the TPC and TFC values between MO extract and MO powder, the values only have a very small difference. Thus, this confirms that the phenolics and quercetin content remained the same before and after freeze-drying.

3.3. MO Leaves Extract: DPPH and ABTS

The percentage of antioxidant activities, which were determined by using DPPH and ABTS assays, the obtained values are 91.68% and 85.1% respectively. The values were slightly lower than the findings obtained by Marimuthu *et al.* [11], which are 96.01% for DPPH and 93% for ABTS. Since the extraction method, storage condition, pretreatment method, and MO tree were the same as Marimuthu *et al.* [11], the potential factors that influence antioxidant activity are leaf age during collection, harvest condition, and time [20]. MO extract was freeze-dried to become powder form, then evaluated by DPPH and ABTS again. The DPPH value is 94.02%, while it is 89.42% for ABTS. Since the DPPH and ABTS inhibition for MO extract and MO powder are almost the same, it is indicated that the antioxidant activity will not be affected by the freeze-drying process. From Table 2, the obtained DPPH value was lower than the findings obtained by Monisha *et al.* [21] and Abo El-Fadl [22] but higher than other studies. Meanwhile, for the ABTS assay, the value gain in this study was lower than that acquired by [18–20] with ABTS values of 93%, 92.67%, and 97.2%, respectively; however, it was higher compared to Avilés-Gaxiola *et al.* [23].

3.4. Encapsulation Efficiency Measurements

The encapsulation efficiency measurements are crucial for nanoparticles that serve as drug carriers or any other bioactive compounds in the drug delivery system. The encapsulation efficiency indicates the proportion of the drug or active compound that is efficiently entrapped into the nanoparticles [24]. The encapsulation efficiency measurements were carried out on two samples, which are PLA-loaded MO NPs and PLA/MMT-loaded MO NPs to make comparisons between both types of NPs. The% EETPC obtained for PLA-loaded MO NPs and PLA/MMT-loaded MO NPs was 86.63% and 96.27%, respectively. The encapsulation efficiency in NPs with MMT is higher than in NPs without MMT. This pattern can be explained by the structure of the MMT itself. MMT is a type of clay mineral with a layered structure that provides interlayer spaces capable of accommodating drug molecules. Therefore, when incorporated into the NPs, MMT plays the role of the reservoir for drug molecules, which results in higher encapsulation efficiency. Besides that, the surface charge and hydrophobicity enhance the attraction towards MO, which leads to higher encapsulation efficiency. A similar pattern was obtained by Bakre *et al.* [25], where the NPs with the inclusion of MMT yielded higher encapsulation efficiency of curcumin into polymeric (93.24%) compared to NPs without MMT (75%). Sun *et al.* [26] showed that capecitabine-loaded polymeric NPs yielded 84.1% of EE%, while organoclay-included NPs yielded a higher EE% of 90.65%.

Table 2. Bioactive components in MO extract

TPC (mg GAE /g)	TFC (mg QE/g)	DPPH (%)	ABTS (%)	References
372.81	**90.885**	**91.70**	**85.10**	**This study**
313.28	90.268	96.01	93.00	[18]
116.60	72.100	97.00	92.67	[19]
34.20	162.35	-	-	[20]
-	-	66.95	97.20	[17]
-	-	36.68	67.00	[21]
103.06	41.81	-	-	[22]
13.40	4.40	40.60	-	[23]

3.5. MO-loaded MMT/PA NPs Kinetics and Release Mechanisms

3.5.1. *In vitro* release of nanoparticles

Figure 2 depicts the release characteristics for two types of nanoparticles: PLA/MMT-loaded MO and PLA-loaded MO at Ph 2, pH 5.5 and pH 7.4. PLA/MMT-loaded MO NPs (Figure 2a), cumulative drug release at pH 2 is rapid in the early phase, reaching around 80% during the first 40 minutes and stabilising near 100% by 180 minutes. This shows that the acidic environment of the gastric fluid has a major impact on the release of the medication from these NPs, most likely due to greater solubility and diffusion at lower pH levels. At pH 5.5, which mimics blood conditions, the release profile is slightly slower than at pH 2, indicating a regulated release mechanism. The release at pH 7.4, which simulates intestinal conditions, displays the slowest growth, attaining a similar final cumulative release percentage but over a longer period. This slower release rate could be related to the drug's lower solubility and diffusion in a more neutral environment, implying that these NPs could result in sustained release in the intestines.

PLA-loaded MO NPs, on the other hand, have a distinct release pattern (Figure 2b). The release at pH 2 is initially rapid, like PLA/MMT-loaded MO NPs, but the total release rate is slower, reaching around 90% cumulative release by 180 minutes. At pH 5.5, the release is much slower, demonstrating a considerable decrease in drug release rate under blood-mimicking circumstances. At pH 7.4, the release rate is the slowest of the three pH levels, with around 80% cumulative release at the end of the experiment. This shows that PLA-loaded MO NPs have a more noticeable pH-dependent release profile, with the slowest release occurring in neutral to slightly alkaline circumstances.

Overall, the incorporation of MMT in PLA/MMT-loaded MO NPs increases the release rate at lower pH levels while giving a more regulated release in neutral to slightly alkaline settings. This could be attributable to MMT's structural features, which may allow for quicker drug absorption in acidic circumstances while also providing sustained release in less acidic situations. PLA-loaded MO NPs, on the other hand, have a more pH-sensitive release, which may make them suited for applications that require slower drug release in the intestines or bloodstream.

3.5.2. Kinetic Release Mechanisms

The best-fitting kinetic model for each type of nanoparticles is summarized in Table 3, which shows the R^2 values for several kinetic models across different pH levels for PLA/MMT-loaded MO NPs and PLA-loaded MO NPs. The Korsmeyer-Peppas model exhibits the highest R^2 values for PLA/MMT-loaded MO NPs at all pH levels (pH 2, pH 5.5, and pH 7.4), in the order of 0.842, 0.840, and 0.824, respectively. At equivalent pH levels, these values are consistently greater than those for the Zero, First, and Higuchi models. The Korsmeyer-Peppas model is most suited to explain the release kinetics of MO from PLA/MMT-loaded NPs, as indicated by the high R^2 values. This approach is frequently applied to polymeric systems in which a mix of diffusion and erosion, for instance may play a role in the release mechanism. When describing drug release from a polymeric system, Korsmeyer-Peppas takes non-Fickian mechanisms into account [27].

With R^2 values of 0.938, 0.927, and 0.903, respectively, the First-order kinetic model for PLA-loaded MO NPs has the greatest values across all pH levels (pH 2, pH 5.5, and pH 7.4). For the identical pH settings, their values are much higher than those of the Zero, Higuchi, and Korsmeyer-Peppas models. The predominance of the First-order model implies that a concentration-dependent process, in which the rate of release falls exponentially with decreasing active agent concentration, primarily controls the release mechanism for PLA-loaded MO NPs. First-order elimination is the process by which a drug leaves the body at a pace that is proportionate to its concentration [28].

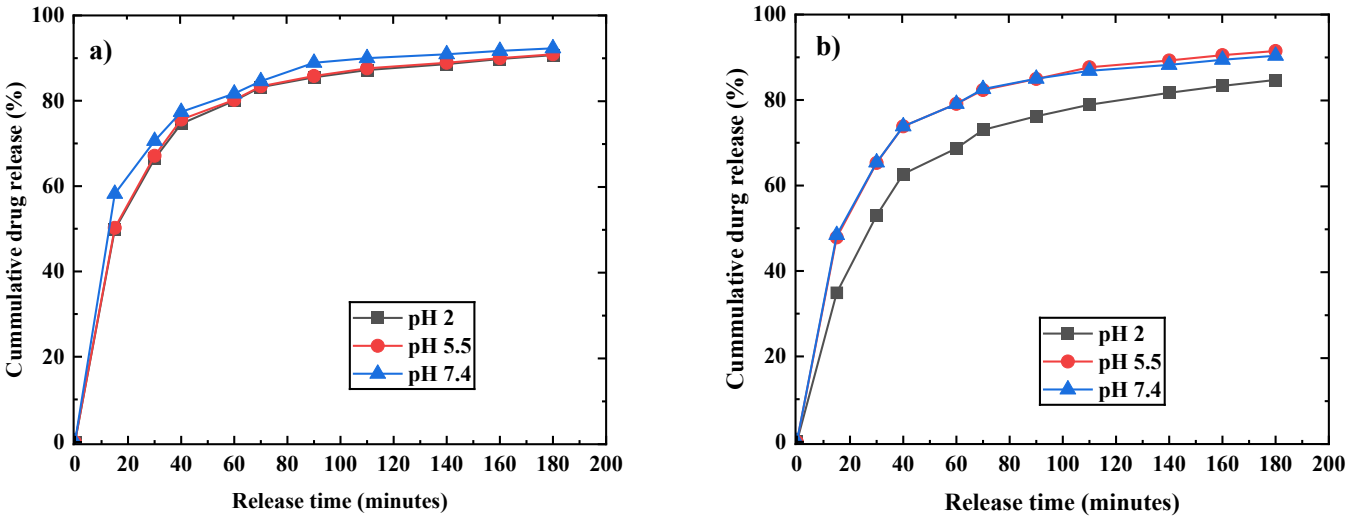

Figure 2. *In vitro* release profiles of (a) PLA/MMT-loaded MO NPs and (b) PLA-loaded MO NPs at pH 2, pH 5.5, and pH 7.4

Table 3. R^2 values for various kinetic models

Kinetic Model	PLA/MMT-loaded MO NPs			PLA-loaded MO NPs		
	R^2 Value			R^2 Value		
	pH 2	pH 5.5	pH 7.4	pH 2	pH 5.5	pH 7.4
Zero	0.831	0.833	0.821	0.755	0.661	0.644
First	0.827	0.824	0.823	**0.938**	**0.927**	**0.903**
Higuchi	0.813	0.808	0.780	0.755	0.661	0.644
Korsemayer-Peppas	**0.842**	**0.840**	**0.824**	0.410	0.362	0.357

3.6. Characterizations of MO-loaded MMT/PLA NPs

3.6.1. FTIR Spectrums

The FTIR spectra in Figure 3 indicate the FTIR spectrums of six (6) different samples: (1) pure MO; (2) pure MMT; (3) pure PLA; (4) physical mixture of MO, MMT, and PLA; (5) PLA/MMT-loaded MO NPs; and (6) MO-loaded PLA NPs. The IR peak of the pure MO sample from line (1) displayed characteristic broad peaks in the region of 3400–3200 cm^{-1}, showing O–H stretching vibrations from hydroxyl groups, which are common in natural products. Peaks at 2920 cm^{-1} indicate C–H stretching vibrations from aliphatic groups, while 1700–1600 cm^{-1} indicates C=O stretching vibrations from carbonyl groups, possibly from aldehydes, ketones, or carboxylic acids. Peaks between 1400 and 1300 cm^{-1} corresponded to C–H bending vibrations, whereas those between 1100 and 1000 cm^{-1} revealed C–O stretching vibrations, indicating the presence of alcohols or carboxylic acids.

The FTIR spectrum of the pure MMT sample, line (2), displayed a clear peak at 3620 cm^{-1}, indicating O–H stretching vibrations inside the clay mineral, and a strong peak at 1040 cm^{-1}, corresponding to Si–O stretching vibrations, which are characteristic of silicate groups. The PLA sample, line (3), showed peaks in the 2995–2945 cm^{-1} range, attributed to C–H stretching vibrations from aliphatic groups. A sharp peak at 1750 cm^{-1} was identified, representing C=O stretching vibrations from ester groups.

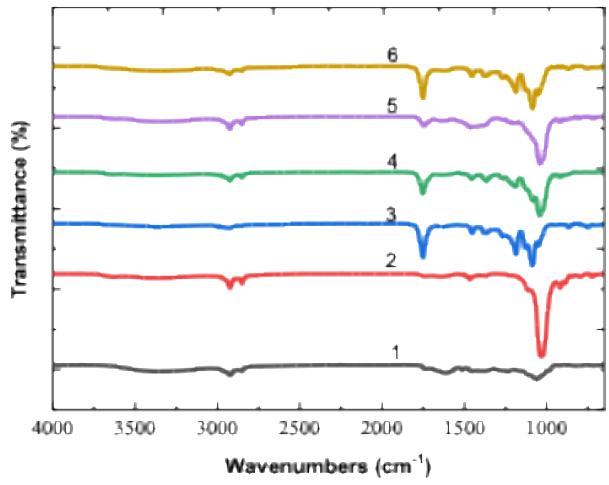

Figure 3. FTIR spectrums of (1) pure MO; (2) pure MMT; (3) pure PLA; (4) physical mixture of MO, MMT, and PLA; (5) PLA/MMT-loaded MO NPs; and (6) MO-loaded PLA NPs

Peaks between 1180 and 1090 cm^{-1} were attributed to C–O–C stretching vibrations, which are indicative of the ester bond in PLA. As a comparison, the physical mixture of MO, MMT, and PLA, line (4), exhibited all the separate components' distinctive peaks. The spectrum revealed broad O–H stretching vibrations around 3400–3200 cm^{-1} from both MO and MMT, C–H stretching vibrations at 2995–2945 cm^{-1} from PLA, a C=O stretching peak at 1750 cm^{-1} from PLA, a Si–O stretching peak at 1040 cm^{-1} from MMT, and C–O stretching vibrations between 1100–1000 cm^{-1} from MO. The spectra show the presence of the individual components' functional groups, with the physical mix and nanoparticle formulations exhibiting combined features but no substantial new peaks, implying that the components are physically mixed rather than chemically linked.

The FTIR spectra of the composite sample, PLA/MMT-loaded MO NPs (line 5), revealed a broad O–H stretching vibration peak in the region of 3400–3200 cm^{-1}, which likely originated from both MO and MMT. The spectra revealed peaks at 2995–2945 cm^{-1} for C–H stretching vibrations from PLA, 1750 cm^{-1} for C=O stretching vibrations from PLA ester groups, 1040 cm^{-1} for Si–O stretching from MMT, and 1100–1000 cm^{-1} for C–O stretching vibrations of MO. Similarly, the PLA-loaded MO NPs, line (6) spectrum, showed O–H stretching vibrations around 3400–3200 cm^{-1}, C–H stretching vibrations at 2995–2945 cm^{-1}, C=O stretching at 1750 cm^{-1}, and C–O stretching vibrations between 1100–1000 cm^{-1}, indicating the presence of both MO and PLA components. These data support the successful encapsulation and interaction of the components in the composite samples, revealing the production of composite nanoparticles for both PLA/MMT-loaded MO NPs and PLA-loaded MO NPs.

3.6.2. X-ray Diffraction Analysis (XRD)

Figure 4 depicts the X-ray diffraction (XRD) patterns of the samples, which include six (6) different samples: (1) pure MO; (2) pure MMT; (3) pure PLA; (4) physical mixture of MO, MMT, and PLA; (5) PLA/MMT-loaded MO NPs; and (6) MO-loaded PLA NPs. The XRD pattern of pure MO (pattern 1) reveals broad peaks at around $2\theta = 20°$, indicating the amorphous nature of the MO extract. This large peak corresponds to the presence of disordered cellulose and other organic molecules found in plant material. The XRD pattern of pure MMT (line 2) shows peaks at $2\theta = 8.8°$, which corresponds to the (001) plane of MMT, and another peak at $2\theta = 19.8°$. These peaks confirm the crystalline nature of MMT clay [29].

Pure PLA (pattern 3) has a large XRD peak at 2θ = 16.7°, indicating its semi-crystalline structure. This peak is related to crystalline portions of the PLA polymer matrix. The physical mixture of MO, MMT, and PLA (pattern 4) demonstrates the combined properties of the constituent components. The pattern exhibits the typical peaks of MMT at 2θ = 8.8° and 19.8°, as well as the broad peak of PLA at 2θ = 16.7°. The presence of a large peak of MO at 2θ = 20° suggests that all three components coexist without considerable interaction at the crystalline level.

The XRD pattern of PLA/MMT-loaded MO NPs (line 5) indicates that the distinctive peaks have shifted and broadened. MMT peaks at 2θ = 8.8° and 19.8° show modest change, showing MO and PLA intercalation inside the layers. PLA's broad peak at 2θ = 16.7° is less pronounced, indicating a decrease in crystallinity caused by the creation of a more amorphous structure in the presence of MO and MMT. The XRD pattern of PLA-loaded MO NPs (pattern 6) shows a broad peak at 2θ = 16.7°, like pure PLA but with lower intensity. This suggests that incorporating MO into the PLA matrix reduces the crystallinity of PLA, resulting in a more amorphous structure, as obtained by Delpouve *et al.* [30] and our previous work [29]. The XRD study indicates the effective encapsulation and interaction of MO with MMT and PLA in nanoparticle formulations. The shifts in peak positions and intensities suggest the creation of novel structures with changed crystallinity, which is critical for understanding the material properties and potential uses of MO-loaded nanoparticles.

Diffusion-controlled (Fickian) or anomalous (non-Fickian) release mechanisms are frequently the result of NP encapsulation, as demonstrated by FTIR and supported by XRD, which shows molecule dispersion or amorphization. Kinetic models such as Korsmeyer-Peppas reflect the fact that the release is controlled by matrix swelling, diffusion, and occasionally erosion due to the lack of strong chemical bonds (physical encapsulation) [31, 32].

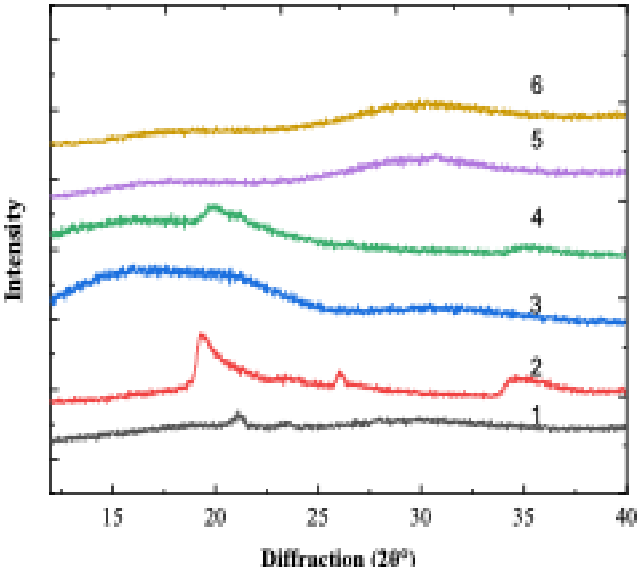

Figure 4. X-ray diffractograms ;(1) pure MO; (2) pure MMT; (3) pure PLA; (4) physical mixture of MO, MMT, and PLA; (5) PLA/MMT-loaded MO NPs; and (6) MO-loaded PLA NPs.

3.6.3. Surface Morphology of MO-loaded MMT/PLA NPs

Figure 5 presents SEM images ofsamples: PLA/MMT-loaded MO NPs, PLA-loaded MO NPs, and blank PLA NPs. The shape and dispersion of nanoparticles within the poly(D,L-lactide) (PLA) matrix can have a substantial impact on the material properties, and these photos offer crucial insights into this process. Blank PLA (Figure 5a) reveals a largely flat surface with a few dispersed particles. Most of the surface is uniform, suggesting that there are no significant additions or fillers present. This consistency is a feature of pure PLA, a substance that has not been improved or altered. The image's enlarged inset (1 µm scale) confirms that there are no notable microstructural characteristics or particle inclusions, indicating that the Blank PLA sample retains its usual polymeric structure unaltered or improved. The same particle size was obtained in our previous work [29], where the $Z_{average}$ was detected at 265 ± 24 n, using Dynamic Light Scattering (DLS) analysis.

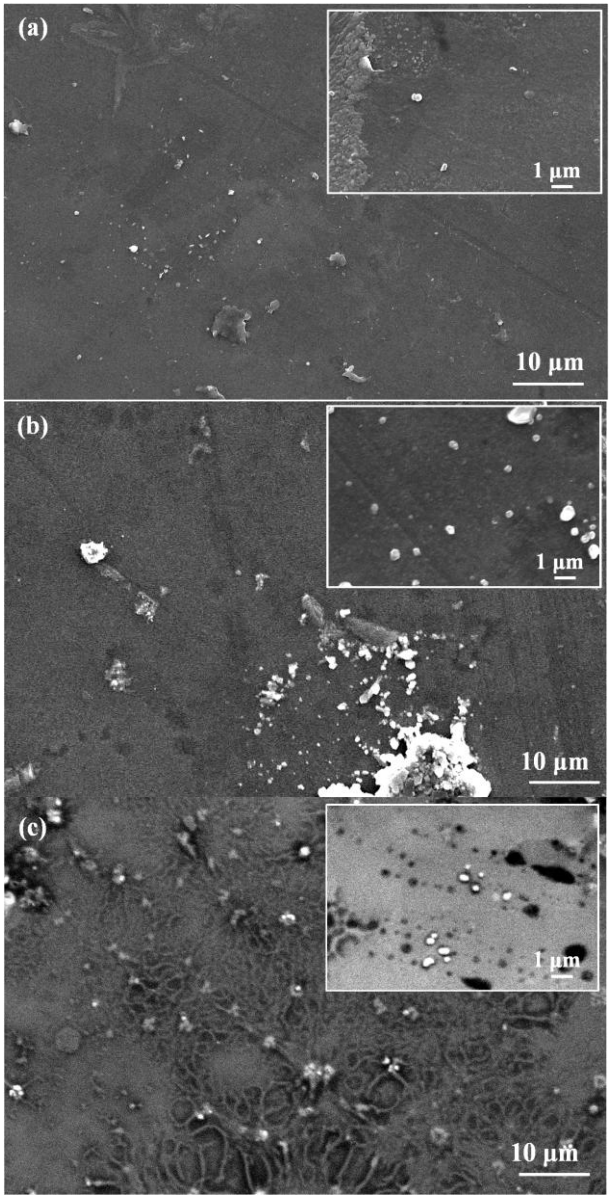

Figure 5. SEM images of: (a) Blank PLA, (b) PLA/MMT-loaded MO NPs and (c) PLA-loaded MO NPS. The inserted pictures are for the high magnification (1 µm) images of each sample

In contrast, the SEM image of the PLA/MMT-loaded MO NPs composite (Figure 5b) reveals a different morphology. The surface of this sample appears more textured, and irregular compared to the blank PLA. The presence of *MO* and MMT nanoparticles is evident, as indicated by the increased roughness and the visible particles dispersed within the PLA matrix. The magnified inset (1 μm scale) shows clusters and individual nanoparticles embedded within the polymer, suggesting a successful incorporation of these additives. The enhanced surface area and the interaction between the PLA matrix and the nanoparticles could contribute to improved mechanical and thermal properties of the composite material.

Meanwhile, PLA-loaded MO NPs (Figure 5c) emphasises the impact of the nanoparticle integration even more. Compared to the PLA/MMT-loaded MO NPs sample, this image reveals a surface with even more noticeable roughness and the presence of bigger agglomerates. There are observable clusters of the nanoparticles dispersed throughout the matrix, suggesting a less uniform distribution. These agglomerates were more visible in the magnified inset (1 μm scale), suggesting that there may have been a probable agglomeration of nanoparticles. The morphology indicates that although the MO nanoparticles are incorporated into the PLA, their dispersion could not be as uniform as it was in the sample of MO NPs loaded with PLA and MMT, which could have an impact on the overall characteristics of the composite.

The inclusion of MO and MMT nanoparticles gives the composite samples a discernible roughness and texture, although the Blank PLA stays smooth and uniform. In contrast to the PLA-loaded MO NPs sample, which displays bigger agglomerates, the PLA/MMT-loaded MO NPs sample displays a more uniform dispersion of nanoparticles. The physical characteristics of the composites, such as their mechanical strength, thermal stability, and possibly even biodegradability, are directly affected by these morphological variations, making them crucial.

4. CONCLUSIONS

The extracted MO leaves were subjected to total phenolic content (TPC) and total flavonoid content (TFC) analyses. The TPC and TFC values obtained were 300.65 μg·QE·mg^{-1} and 92.15 μg·QE·mg^{-1}, respectively. Encapsulation efficiency measurements were conducted on the two types of NPs synthesized, which are the PLA loaded-MO NPs, and PLA/MMT loaded-MO NPs. The encapsulation efficiency obtained from the two samples was 86.63% and 96.27%, respectively. PLA/MMT loaded-MO NPs achieved higher encapsulation efficiency, attributed to the incorporation of MMT which plays the role of as reservoir for drug molecules which increases the encapsulation rate.

FTIR analysis resulted in a significant decrease around the wavenumber of 1100 to 1200 cm^{-1} due to the encapsulation of MO and MMT into the NPs. SEM images presented discrete nanospheres for blank PLA NPs, and PLA loaded-MO NPs while PLA/MMT loaded-MO NPs had a slightly irregular shape due to the incorporation of MMT. Encapsulation efficiency measurements demonstrated that PLA/MMT loaded MO NPS NPs exhibited high efficiency, owing to MMT that acts as a reservoir for enhanced encapsulation. MO release experiments in PBS solutions (pH 2.0, 5.5, and 7.4) revealed that MMT slowed the release rate and reduced the initial burst volume of MO from the polymer matrix. Mathematical modeling (zero-order, first-order, Higuchi, and Korsmeyer-Peppas) identified the Korsmeyer-Peppas model as the best fit, indicating non-Fickian diffusion in all tested pH conditions (2.0, 5.5, and 7.4) for both NPs samples. In summary, the study successfully demonstrated the preparation, characterization, and drug release behavior of PLA/MMT-loaded MO NP incorporating MO extract, highlighting their potential application in controlled release systems.

ACKNOWLEDGMENTS

The authors gratefully acknowledge the financial support given for this work through the FRGS/1/2021/TK0/ UNIMAP/02/11 grant.

REFERENCES

[1] P. Purnama, Z. S. Saldi, and M. Samsuri, “The Development of Polylactide Nanocomposites: A Review,” *Journal of Composites Science*, vol. 8, no. 8, p. 317, 2024.

[2] R. Othman, G. Vladisavljević, N. Thomas, and Z. Nagy, “Fabrication of Composite Poly(ᴅ,ʟ-Lactide)/ Montmorillonite Nanoparticles for Controlled Delivery of Acetaminophen by Solvent-Displacement Method using Glass Capillary Microfluidics,” *Colloids and surfaces B: Biointerfaces*, vol. 141, pp. 187–195, 2016.

[3] H. Yan *et al.*, “Synthesis and assessment of CTAB and NPE modified organo-montmorillonite for the fabrication of organo-montmorillonite/alginate based hydrophobic pharmaceutical controlled-release formulation,” *Colloids and Surfaces B: Biointerfaces*, vol. 191, p. 110983, 2020.

[4] M. L. Bello *et al.*, “Development of novel montmorillonite-based sustained release system for oral bromopride delivery.,” *European Journal of Pharmaceutical Sciences*, vol. 175, p. 106222, 2022.

[5] A. Anzano *et al.*, “Chemical Analysis and Antimicrobial Activity of *Moringa oleifera* Lam. Leaves and Seeds,” *Molecules*, vol. 27, no. 24, p. 8920, 2022.

[6] N. Shah, M. Kumari, P. Sadhu, C. Talele, H. Rajput, and R. Sapra, “Nano-Herbal Innovations: Precision in Therapeutic Delivery,” *Journal of Advanced Zoology*, vol. 45, pp. 576–581, 2024.

[7] S. Ai *et al.*, “Collision of herbal medicine and nanotechnology: a bibliometric analysis of herbal nanoparticles from 2004 to 2023,” *Journal of Nanobiotechnology*, vol. 22, p. 140, 2024.

[8] J. Jenifer and R. T. P. Upputuri, “In vitro release mechanism and cytotoxic behavior of curcumin loaded casein nanoparticles,” *Brazilian Journal of Pharmaceutical Sciences*, vol. 58, p. e19801, 2022.

[9] Y. Cui, Y. Liu, Q. Zhang, and Y. Liu, “Controlled Release Mechanism of Thymol Loaded into Mesoporous Silica

Nanoparticles for Active Packaging Films," *Food Bioscience*, vol. 56, p. 103229, 2023.

[10] E. Okka, T. Tongur, T. Aytas, M. Yılmaz, Ö. Topel, and R. Sahin, "Green Synthesis and the Formation Kinetics of Silver Nanoparticles in Aqueous *Inula Viscosa* Extract," *Optik*, vol. 294, p. 17148, 2023.

[11] L. F. Ang, D. Yusrida, Y. P. Lip, and F. Y. Mun, "Microencapsulation Curcuminoids for Effective Delivery in Pharmaceutical Application," *Pharmaceutics*, vol. 11, no. 9, p. 451, 2019.

[12] E. Jara-Quijada *et al.*, "Liposomes Loaded with Green Tea Polyphenols—Optimization, Characterization, and Release Kinetics Under Conventional Heating and Pulsed Electric Fields," *Food and Bioprocess Technology*, vol. 17, pp. 396–408, 2024.

[13] M. D. E. S. Marimuthu, R. Othman, S. P. M. Bohari, and W. J. Ooi, "Intensification of Antioxidant-Rich Extract from *Moringa Oleifera* Leaves Using Different Solvents: Optimization and Characterization," in *Emerging Technologies for Future Sustainability*, H. Shukor, H. N. A. Halim, H. L. Ong, B.-B. Lee, and M. H. M. Pisal, Eds., Singapore: Springer Nature Singapore, 2023, pp. 359–374.

[14] R. Wołosiak *et al.*, "Verification of the Conditions for Determination of Antioxidant Activity by ABTS and DPPH Assays—A Practical Approach," *Molecules*, vol. 27, no. 1, p. 50, 2021.

[15] E. Jamróz, P. Kulawik, and P. Kopel, "The Effect of Nanofillers on the Functional Properties of Biopolymer-Based Films: A Review," *Polymers*, vol. 11, no. 4, p. 675, 2019.

[16] C. Pinto Reis, R. J. Neufeld, António J. Ribeiro, and F. Veiga, "Nanoencapsulation I. Methods for preparation of drug-loaded polymeric nanoparticles," *Nanomedicine: Nanotechnology, Biology and Medicine*, vol. 2, no. 1, pp. 8–21, 2006.

[17] R. Othman, G. T. Vladisavljević, H. Shahmohamadi, Z. K. Nagy, and R. G. Holdich, "Formation of Size-Tuneable Biodegradable Polymeric Nanoparticles by Solvent Displacement Method Using Micro-Engineered Membranes Fabricated by Laser Drilling and Electroforming," *Chemical Engineering Journal*, vol. 304, pp. 703–713, 2016.

[18] K. D. R. Ramarao, C. Somasundram, Z. Razali, W. Kunasekaran, and T. Li Jin, "The antioxidant properties and microbial load of *Moringa oleifera* leaves dried using a prototype convective air-dryer," *Saudi Journal of Biological Sciences*, vol. 29, no. 6, p. 103290, 2022.

[19] R. Albarri and S. Şahin, "A green method for the extraction of *Moringa oleifera* leaves: evaluation of several in vitro assays for bioactive properties," *Biomass Conversion and Biorefinery*, vol. 14, no. 5, pp. 6397–6405, 2024.

[20] M. Gómez-Martínez *et al.*, "Location and Tissue Effects on Phytochemical Composition and *In Vitro* Antioxidant Activity of *Moringa oleifera*," *Industrial Crops and Products*, vol. 151, p. 112439, 2020.

[21] M. Devi, R. Othman, M. I. H. M. Dzahir, and S. P. M. Bohari, "Formation of Bioresorbable PCL-Loaded *Moringa Oleifera* L./Natural Clay Functional Particles by Solvent Displacement Method for Pharmaceutical Applications," in *Proceedings of the 3rd International Conference on Biomass Utilization and Sustainable Energy; ICoBiomasSE 2023; 4–5 September; Kuala Lumpur, Malaysia*, H. L. Ong, S. J. H. M. Yusof, K. F. Kasim, A. A. N. Gunny, and R. Othman, Eds., Singapore: Springer Nature Singapore, 2024, pp. 101–113.

[22] S. Abo El-Fadl, A. Osman, A. Al-Zohairy, A. Dahab, and Z. Abo El Kheir, "Assessment of Total Phenolic, Flavonoid Content, Antioxidant Potential and HPLC Profile of Three Moringa Species Leaf Extracts," *Scientific Journal of Flowers and Ornamental Plants*, vol. 7, no. 1, pp. 53–70, 2020.

[23] S. Avilés-Gaxiola *et al.*, "Antioxidant and Anti-Inflammatory Properties of Novel Peptides from *Moringa oleifera* Lam. Leaves," *South African Journal of Botany*, vol. 141, pp. 466–473, 2021.

[24] A. Kumari, R. Singla, A. Guliani, and S. K. Yadav, "Nanoencapsulation for Drug Delivery," *EXCLI Journal*, vol. 13, pp. 265–286, 2014.

[25] L. G. Bakre, J. I. Sarvaiya, and Y. K. Agrawal, "Synthesis, Characterization, and Study of Drug Release Properties of Curcumin from Polycaprolactone/ Organomodified Montmorillonite Nanocomposite," *Journal of Pharmaceutical Innovation*, vol. 11, pp. 300–307, 2016.

[26] S. B. Sun, P. Liu, F. M. Shao, and Q. L. Miao, "Formulation and Evaluation of PLGA Nanoparticles Loaded Capecitabine for Prostate Cancer," *International Journal of Clinical and Experimental Medicine*, vol. 8, no. 10, p. 19670, 2015.

[27] N. S. Heredia *et al.*, "Comparative Statistical Analysis of the Release Kinetics Models for Nanoprecipitated Drug Delivery Systems Based on Poly(lactic-co-glycolic acid)," *PLoS One*, vol. 17, no. 3, p. e0264825, 2022.

[28] S. Ranote *et al.*, "Functionalized *Moringa oleifera* Gum as pH-Responsive Nanogel for Doxorubicin Delivery: Synthesis, Kinetic Modelling and *In Vitro* Cytotoxicity Study," Polymers, vol. no. 14, p. 4697, 2022.

[29] R. Othman, G. T. Vladisavljević, N. L. Thomas, and Z. K. Nagy, "Fabrication of composite poly(D,L-lactide)/ montmorillonite nanoparticles for controlled delivery of acetaminophen by solvent-displacement method using glass capillary microfluidics," *Colloids Surface B: Biointerfaces*, vol. 141, pp. 187–195, 2016.

[30] N. Delpouve *et al.*, "Effects of organo-LDH dispersion on thermal stability, crystallinity and mechanical features of PLA." *Polymer*, vol. 208, p. 122952, 2020.

[31] S. A. Mathew and S. Arumainathan, "Crosslinked Chitosan–Gelatin Biocompatible Nanocomposite as a Neuro Drug Carrier," *ACS Omega*, vol. 7, no. 22, pp. 18732–18744, 2022.

[32] O. Sreekanth Reddy, M. C. S. Subha, T. Jithendra, C. Madhavi, and K. Chowdoji Rao, "Curcumin encapsulated dual cross linked sodium alginate/ montmorillonite polymeric composite beads for controlled drug delivery," *Journal of Pharmaceutical Analysis*, vol. 11, no. 2, pp. 191–199, 2021.